

The dehydroxylation of chrysotile: A combined in situ micro-Raman and micro-FTIR study

ROY TRITTSCHACK* AND BERNARD GROBÉTY

Department of Geosciences, University of Fribourg, Chemin du Musée 6, Fribourg CH-1700, Switzerland

ABSTRACT

One of the most important mechanisms releasing water in subducting slabs of oceanic crust is connected to the dehydration of serpentinized oceanic rocks. This study reports on a detailed investigation of the transition from chrysotile—an important serpentine mineral—to forsterite through the release of water.

The dehydroxylation of natural chrysotile and the subsequent phase change to forsterite was studied by in situ micro-Raman and micro-FTIR spectroscopy in the temperature range of 21 to 871 °C. Comparisons were made with previously published data of lizardite-1T. Micro-Raman spectra obtained in the low-frequency (100–1200 cm⁻¹) and high-frequency ranges (3500–3800 cm⁻¹) were complemented by micro-FTIR measurements between 2500 and 4000 cm⁻¹ to study changes in the chrysotile structure as a function of dehydroxylation progress. In general, room-temperature chrysotile bands lie at higher wavenumbers than equivalent bands of lizardite-1T except of three bands positioned at 301.7, 317.5, and 345.2 cm⁻¹. Different band assignments of chrysotile and lizardite-1T Raman spectra from literature are compared. The most striking assignments concern the three aforementioned Raman bands and those lying between 620 and 635 cm⁻¹. The present data support a chrysotile- or at least curved TO layer related origin of the latter. Deconvolution of overlapping OH stretching bands at room temperature revealed the presence of five (FTIR) and four (Raman) bands, respectively. A slight change in the ditrigonal distortion angle α during heating and the effects of a radius-dependent dehydroxylation progress can be shown. Furthermore, it was possible to identify a quenchable talc-like phase immediately after the onset of the dehydroxylation at 459 °C. Main bands of this phase are positioned at 184.7, 359.2, and 669.1 cm⁻¹ and a single OH band at 3677 cm⁻¹, and are thus quite similar to those reported for dehydroxylating lizardite-1T. Their appearance coincides with the formation of forsterite. A maximum in the integral intensity of the talc-like intermediate is reached at 716 °C. At higher temperatures, the intermediate phase breaks down and supports the accelerated growth of forsterite. The lack of OH bands with the concomitant appearance of broad chrysotile-related modes in the low-frequency range after heating the sample to 871 °C indicates the presence of a heavily disordered phase still resembling chrysotile. However, there are no spectral evidences for further Si- and/or Mg-rich amorphous phases during the dehydroxylation and no indications for a relationship between the breakdown of the talc-like phase and the growth of enstatite as previously reported in literature.

Keywords: Chrysotile, dehydroxylation, in situ micro-Raman and micro-FTIR spectroscopy, talc-like intermediate

INTRODUCTION

Chrysotile is a member of the serpentine group with an ideal formula Mg₃Si₂O₅(OH)₄. Common building blocks of this group are octahedrally coordinated (O) brucite-like sheets linked with tetrahedrally coordinated (T) sheets of SiO₄ that form a trioctahedral 1:1 (TO) layer phyllosilicate. The misfit between both sheets gives rise to various modulated polymorphs of the flat layered lizardite, such as antigorite with undulating layers and chrysotile with wrapped cylindrical layers, but also rare species like polygonal and polyhedral serpentine (Wicks and Whittaker 1975; Grob ty 2003; D dony and Buseck 2004; Cressey et al. 2008). X-ray diffraction (XRD) and high-resolution transmission electron microscopy (HRTEM) revealed the existence of different chrysotile polytypes. Known polytypes are clino-, ortho-, and parachrysotile, while clinochrysotile is the most abundant one

(Wicks and O'Hanley 1988).

Physico-chemical properties of chrysotile, e.g., the dehydroxylation temperature, are likely to change with the radius of the fiber owing to slight changes of structural parameters (e.g., bond lengths and angles) with curvature (Evans 2004). This behavior causes a continuous phase transformation starting on the chrysotile wall edges at approximately 450 °C and propagating to the inner wall, where the layers start to dehydroxylate only above 600 °C (Viti 2010). Literature on the thermal behavior of chrysotile is extensive due to the peculiar structure, the excellent heat resistance, and insulating properties of chrysotile (=white asbestos) compounds (e.g., Ball and Taylor 1963; Brindley and Hayami 1963a, 1963b; Martin 1977; Datta et al. 1987; Candela et al. 2007). Early articles by Aruja (1943), Hey and Bannister (1948), and Brindley and Zussman (1957) have studied the phase transformation from chrysotile to forsterite. They observed an amorphous phase as primary product of dehydroxylation, fol-

* E-mail: roy.trittschack@unifr.ch

lowed by forsterite. Their results indicate a topotactic relationship between primary chrysotile and forsterite, despite the intervening amorphous phase. Among others, Brindley and Zussman (1957) also documented the presence of a potential poorly crystalline intermediate phase on the base of a low-angle XRD peak at around 14 Å, shifting to 10 Å with progressive heating. A series of studies also focused on the structure of potential intermediate phase(s) without identifying such phase(s) in detail (Ball and Taylor 1963; Brindley and Hayami 1963a, 1963b; Martin 1977; Jolicoeur and Duchesne 1981; Datta et al. 1987; Datta 1991). Based on nuclear magnetic resonance (NMR) studies, MacKenzie and Meinhold (1994) suggested the occurrence of a talc-like intermediate during “dry” dehydroxylation, which they labeled as “dehydroxylated II.” Talc is a stable product phase during the dehydroxylation of serpentine under hydrothermal conditions (Ball and Taylor 1963; O’Hanley et al. 1989). Among XRD and FTIR results, McKelvy et al. (2004, 2006) made first-principle simulations of the lizardite dehydroxylation process, which gave as product phase an intermediate, “meta-serpentine,” ~14 Å phase, plus an amorphous phase. They explain the formation of the meta-serpentine phase with a lamellar nucleation and growth mechanism leading to a strong topotactic relationship between primary serpentine and the 14 Å phase. Recent studies on the dehydroxylation mechanisms and kinetics of chrysotile and serpentine minerals in general have gained growing interest (Cattaneo et al. 2003; Viti 2010; Gualtieri et al. 2012). This is caused by an enhanced interest in subduction zone seismicity, inertization of asbestiform waste, CO₂ sequestration and the demand for a cost-efficient and simple way to distinguish serpentine polymorphs.

This study presents in situ micro-Raman and micro-FTIR investigations of the dehydroxylation of chrysotile, which will be compared with recently published data on the dehydroxylation of lizardite-1T (Trittschack et al. 2012).

EXPERIMENTAL METHODS

Sample material

The investigated chrysotile sample was taken from a chrysotile vein in a serpentinite of the mineral collection of the University of Fribourg, Switzerland, without details of origin (internal reference chry 33/12). Transmission electron microscopy based energy-dispersive spectroscopy (TEM-EDS) experiments yield 51.2 wt% MgO, 48.0 wt% SiO₂, and 0.1 wt% FeO^{tot}, which fits an almost pure Mg end-member. The resulting XRD spectrum is close to the ICDD reference patterns 25-0645 and 10-0381 of clinochrysotile and shows no additional peaks (Fig. 1). Selected-area electron diffraction (SAED) patterns are compatible with XRD data and exclude the presence of parachrysotile (Fig. 2), although it is not possible to distinguish clearly between clino- and orthochrysotile. HRTEM based measurements of the outer diameter gives values between 23 and 85 nm, but more than 75% of the measured fibers lie in the range between 30 and 60 nm.

As a reference for the interpretation of the chrysotile Raman measurements, spectra of a lizardite-1T single crystal from the Monte Fico quarries, Elba Island, Italy, were used (private collection, Marcello Mellini). Mellini and Viti (1994) and Fuchs et al. (1998) provided comprehensive mineralogical and chemical data of this sample.

Raman and FTIR experiments were carried out on sub-parallel fiber bundles positioned in a heat-resistant sapphire crucible. The Monte Fico single crystal was independently measured in the same sapphire crucible with an orientation *c* parallel to the incident Raman laser beam.

FTIR and Raman spectroscopy

Micro-FTIR measurements were performed with a Bruker VERTEX 80v spectrometer attached to a Hyperion1000 FTIR microscope at the GeoForschungsZentrum

Potsdam (GFZ Potsdam/Germany). Spectra were collected in the 2500–4000 cm⁻¹ frequency range using a LN-INSB D413 detector, a KBr beamsplitter and a 6 mm aperture in transmission mode. Each spectrum was measured with a resolution of 2 cm⁻¹ and averaged over 60 individual scans resulting in a measurement interval of about 64 s. A 10 × 40 μm sized area of sub-parallel fibers was chosen to collect FTIR spectra of chrysotile.

Micro-Raman investigations were carried out with a HORIBA HR 800 UV spectrometer (grating 1800 grooves/mm, focal length 800 mm, 1024 × 256 pixel CCD detector) connected to a XY adjustable stage and an Olympus BX41 microscope (20× objective, backscattering configuration) at the GFZ Potsdam. A confocal pinhole of 100 μm was used for all measurements. The Raman setup used offers a spectral resolution of about 1 cm⁻¹. The Raman spectrometer was run with an argon laser (488 nm, 300 mW) and calibrated against the emission bands of a neon lamp. The illuminated diameter on the sample surface yields 4.4 μm considering the used Raman setup. Spectra acquisition time was 40 s and 3 spectra were cumulated for each temperature step. In general, spectra were measured in the frequency range of 100–1200 and 3500–3800 cm⁻¹.

In situ high-temperature (HT) micro-FTIR and micro-Raman measurements were performed by using a software-controlled Linkam TS1000 heating stage placed onto the FTIR and Raman microscope stage. The thermocouple was calibrated using the melting points of different salts: NaNO₃ (*T_M* = 306 °C), NaI (*T_M* = 651

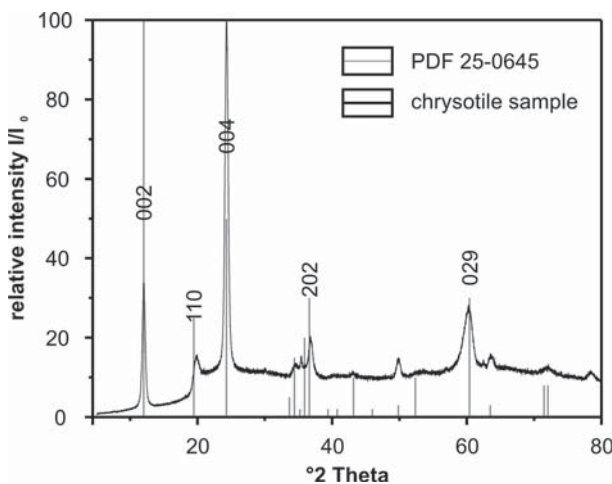


FIGURE 1. X-ray powder diffraction pattern of the studied chrysotile sample chry 33/12 compared with the ICDD entry 25-0645.

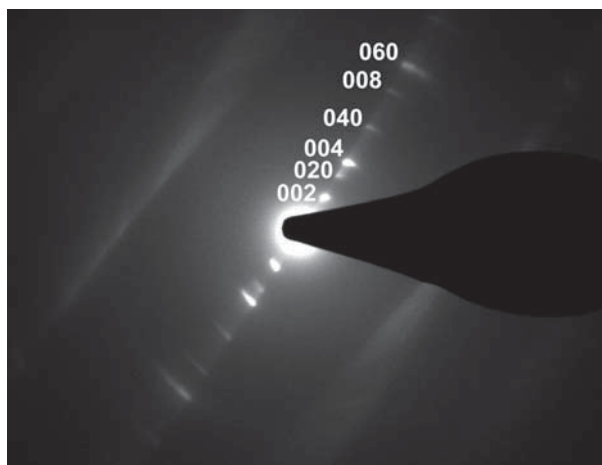


FIGURE 2. SAED pattern of chrysotile. Strong reflections are compatible with the clino- and orthochrysotile polytypes.

°C), and NaCl ($T_M = 801$ °C). The 0 °C point was included in the calibration line. To guarantee a rapid removal of the water generated during the dehydroxylation a constant flow of nitrogen was adjusted.

FTIR spectra of chrysotile were successively measured at 21, 98, 201, 304, 356, 407, 433, and 459 °C with a constant heating rate of 130 °C/min between the respective temperatures. For temperatures higher than 459 °C an automated measuring/heating cycle was programmed up to a maximum temperature of 871 °C (heating rate $\beta = 1$ °C/min, single acquisition time 64 s). Raman data of one single fiber bundle were subsequently acquired at 21, 47, 98*, 150*, 201*, 253*, 304*, 356*, 407*, 459*, 484, 510*, 562, 587, 613*, 639, 665*, 690, 716, 768*, and 871* °C. The dwell time amounts to around 8 min at the respective temperatures owing to the experimental conditions. The heating rate between each temperature level was fixed at $\beta = 100$ °C/min. Additional low-temperature spectra, referred as “quenched” data, were taken from samples heated to temperatures marked by an asterisk after cooling them down to 47 °C. Afterward the sample was heated up to the next higher temperature. Thus, the chrysotile bundle were cyclically heated and T -quenched several times, which result in a total experiment duration of around 8.5 h. The stability of the Raman shift was checked by an artificial, non-sample related band at 416.8 cm⁻¹ at RT (Fig. 3).

The Raman spectra were corrected for temperature- and frequency-dependent scattering intensity by the method provided by Long (1977). Afterward, the Raman intensities were normalized to the temperature providing the greatest absolute intensity.

Fitting procedure

PeakFit (v4.12) was used to perform peak deconvolution and integration of all FTIR and Raman spectra. The low-frequency range (100–1200 cm⁻¹) and high-frequency range (3500–3800 cm⁻¹) of the Raman data were treated independently. Spectra smoothing was done by the implemented Savitzky-Golay algorithm. After baseline subtraction (linear baseline), all spectra were fitted using a combined Gaussian-Lorentzian Amplitude function with the base and the full-width at half maximum (FWHM) as refinable parameters. A minimum number of peaks was chosen to guarantee a best fit as shown by Auzende et al. (2004).

RESULTS

Raman and FTIR spectra at ambient conditions

The chrysotile sample was measured at ambient conditions in the low-frequency range (100–1200 cm⁻¹). A comparison with the Monte Fico lizardite-1T and a reference spectrum of chrysotile from the RRUFF database (Downs 2006) is shown in Figure 4. Five major bands are located at 129.3, 233.3, 389.4, 691.3, and 1105.4 cm⁻¹, which are accompanied by a series of less intense

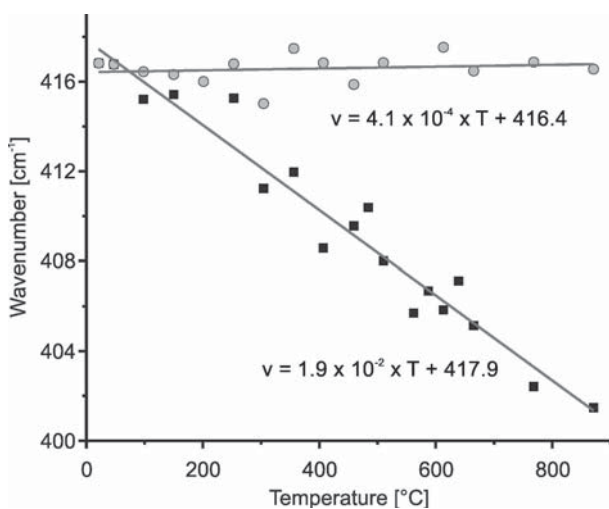


FIGURE 3. Temperature-dependent evolution of the Raman shift of an external, non-sample related artifact for observing the stability of the Raman setup with time and temperature.

band (Fig. 4; Table 1). In general, all low-frequency bands are in good agreement with the RRUFF reference spectrum R070088 of chrysotile (Downs 2006) and data reported by Klopogge et al. 1999, Rinaudo et al. (2003), and Auzende et al. (2004). Compared with lizardite-1T (Trittschack et al. 2012), chrysotile bands lie at higher wavenumbers than equivalent lizardite modes (Fig. 4, Table 1).

Three bands at 301.7, 317.5, and 345.2 cm⁻¹ whose assignments are still under discussion (Farmer 1974; Klopogge et al. 1999; Hofmeister and Bowey 2006) are an exception to this rule. They are located at lower wavenumbers with respect to the equivalent bands of lizardite-1T (Trittschack et al. 2012). Highly sensitive deformation modes of SiO₄-AlO₄ as reported for the Monte Fico lizardite sample and antigorite (Rinaudo et al. 2003; Trittschack et al. 2012) are not present, which is compatible with the TEM-EDS based aluminum free composition of the analyzed chrysotile sample. The most significant difference between lizardite and chrysotile occurs in the region of the antisymmetric Si-O stretching modes. Whereas lizardite shows at least two bands belonging to ν_{as} Si-O_{nb} and ν_{as} Si-O_b-Si, chrysotile shows only one detectable band assigned to ν_{as} Si-O_{nb}, i.e., an antisymmetric stretching mode perpendicular to the tetrahedral sheet (Klopogge et al. 1999).

The high-frequency range (3500–3800 cm⁻¹) is characterized by hydroxyl stretching vibrations that are listed and compared with that of lizardite-1T in Table 1. The RT band deconvolution

TABLE 1. Raman bands of chrysotile and lizardite-1T and their assignments at room temperature

Band assignment*†‡	Chrysotile§ (cm ⁻¹)	Chrysotile (cm ⁻¹)	Lizardite-1T# (cm ⁻¹)
O-Si-O bending mode	129.3		129.4
A _{1g} mode of Mg(O,OH) ₆	201.9	199	201.9
Vibrations of O3-H3...O2	233.3	231	229.1
Bending of SiO ₄	301.7	304	305.1
	317.5	318	320.0
	345.2	345	346.2
s Mg-OH vibrations		374	371.4
s ν_2 (e) SiO ₄	389.4	388	383.5
unknown artefact	416.8		
as Mg-OH translation	432.4	432	430.4
ν_3 (a ₁) SiO ₄	455.1	458	
Mg-OH translation + ν_6 (e) SiO ₄	467.6	466	464.5
Libration of inner Mg-OH		607	
as OH-Mg-OH translation modes	623.3	622	621.6
		629	
ν_2 Si-O _b -Si	691.3	692	689.8
Mg-OH outer s translation modes	706.5	705	707.1
		709	
Si-O stretching			928.6
			972.4
ν_{as} Si-O _b -Si			1050.2
ν_{as} Si-O _{nb}	1105.4	1102	1094.3
OH stretching frequencies			
Out-of-phase of inner surface OH	3649	3643	3649
Unassigned OH band			3670
In-phase inner surface OH	3681	3678	3684
	3688	3686	3691
Inner OH	3697	3696	3698
			3704

Note: as = antisymmetric, s = symmetric, b = bridging, nb = non-bridging.

* Rinaudo et al. (2003).

† Farmer (1974).

‡ Klopogge et al. (1999).

§ Balan et al. (2002).

|| This work.

Trittschack et al. (2012).

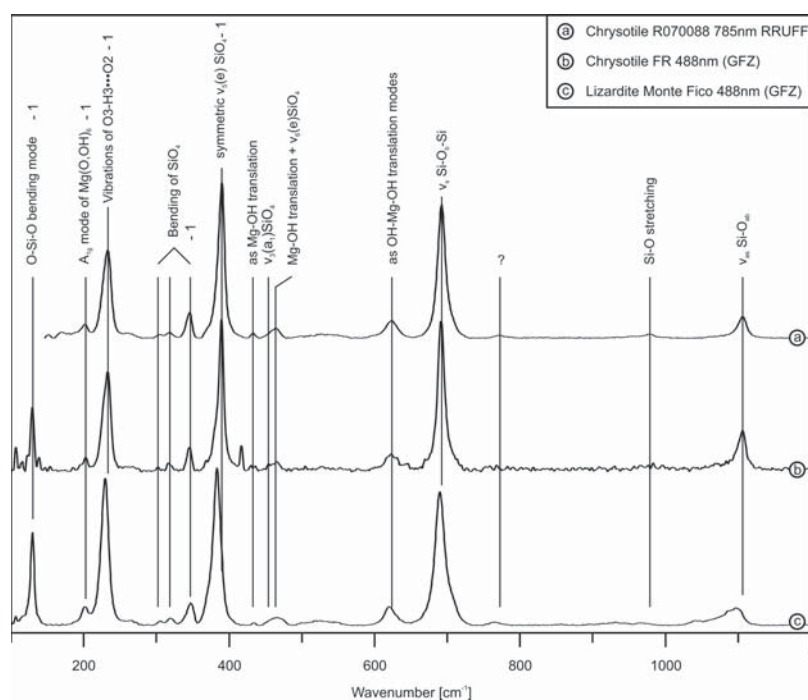


FIGURE 4. Comparison between the Raman spectrum of the chrysotile studied and the chrysotile reference spectrum R070088 (Downs 2006) as well as the Monte Fico lizardite-1T spectrum (Trittschack et al. 2012); 1 = marks those bands that were followed during heating to demonstrate the band shifting as shown in Figure 7.

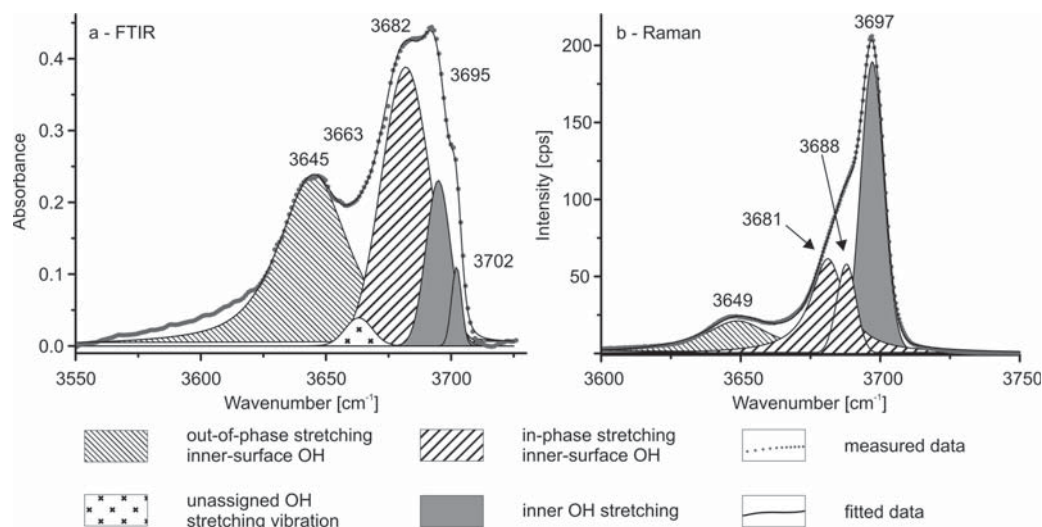


FIGURE 5. Band deconvolution of the OH stretching modes at RT and their assignments following Balan et al. (2002) and Auzende et al. (2004).

(Fig. 5) gives five IR (3645, 3663, 3682, 3695, and 3702 cm^{-1}) and four Raman bands (3649, 3681, 3688, and 3697 cm^{-1}), respectively. The shape and the relative intensity/absorbance of single OH stretching bands differ considerably between Raman and FTIR spectra. Thus, the Raman spectrum contains four bands as proposed by Kloprogge et al. (1999), but the two additional bands (six in total) reported by Auzende et al. (2004) were not observed. Contrary to that, there is a higher number of infrared (IR) active bands, i.e., five compared to

two, as formerly reported (Farmer 1974; Post and Borer 2000; Anbalagan et al. 2010). Similar observations were already made in spectroscopic investigation of lizardite-1T (Trittschack et al. 2012), i.e., there are more IR bands, but less Raman bands than reported in the literature. Band assignments were made using the scheme of Balan et al. (2002) for lizardite and its application proposed for other serpentine polymorphs (Auzende et al. 2004). Adjacent bands are interpreted as originating from the same mode.

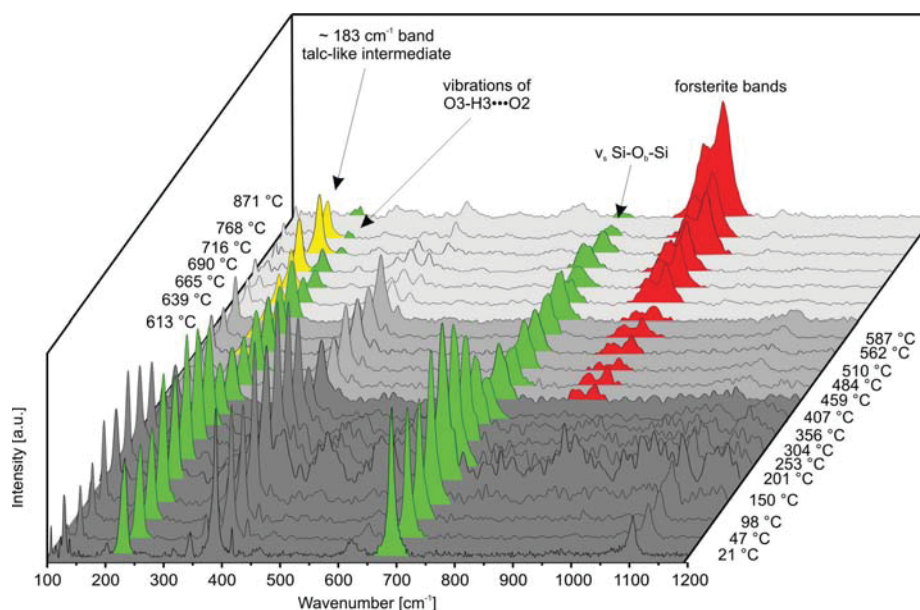
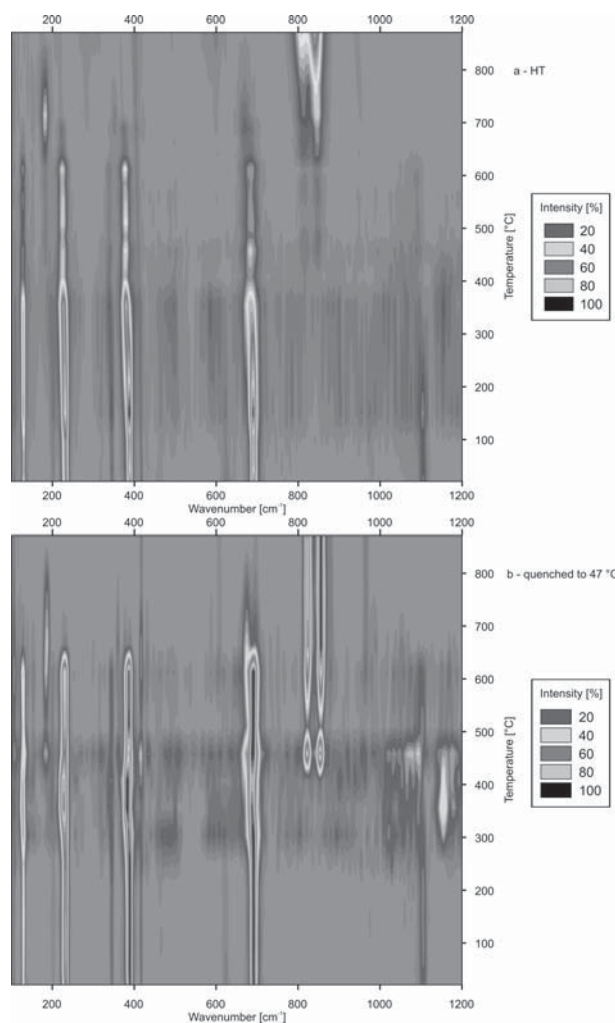


FIGURE 6. Temperature-dependent evolution of the low-frequency Raman bands between 21 and 871 °C. Some bands are color-coded for clarity: green = chrysotile, yellow = transition phase, and red = forsterite modes.

High-temperature FTIR and Raman spectroscopy of the dehydroxylation of chrysotile

The treatment and interpretation of the in situ HT spectra of chrysotile were done in similar manner as for lizardite-1T by Trittschack et al. (2012) to show differences related to the polymorphic character of both serpentine minerals. Only strong bands (Fig. 4) were followed in detail during the temperature treatment because of band broadening and a rapid decrease of the signal-to-noise ratio with increasing temperature. A major increase of the background intensity is present in the spectra measured at 201 to 356 °C (Fig. 6). In general, the frequency of all chrysotile modes in the low-frequency range shows a negative dependence on temperature in the HT as well as the quenched data. Individual Raman bands such as the A_{1g} mode (201.9 cm^{-1} at RT) and the symmetrical stretching mode of Si-O_b-Si (691.3 cm^{-1} at RT) are additionally characterized by band splitting at 459 °C, with a new band appearing at lower wavenumbers than that of the existing band (Figs. 6, 7a–7b, and 8). A common feature of all studied bands preventing a linear fit across the entire temperature range is a rapid shift down to a minimum in wavenumber position at 356 and 407 °C before going slightly up again at $T \geq 459$ °C, i.e., the temperature at which first forsterite bands are visible. Above this temperature there might be a plateau or even a decelerated shift up to $T = 665$ °C, especially in data of the O3-H3...O2 and the sym $\nu_3(e)$ SiO₄ modes. Afterward, individual bands shift again to lower wavenumbers and disappear almost completely due to a fast decrease in intensity. There is a considerable difference in the total amount of temperature-dependent frequency change when comparing the O-Si-O bending mode (Fig. 8a) with all other modes shown in Figure 8.

► FIGURE 7. (a and b) Temperature-dependent band evolution of Raman band intensity. (a) Measured at HT and (b) measured from samples quenched from the indicated temperatures to 47 °C.



The integral intensity/absorbance of the chrysotile modes in the low-frequency range are characterized by a stepwise decrease. Major steps occur between 356 and 407 °C (Raman data) as well as 613 and 639 °C (Raman and FTIR data). The first intensity decrease is accompanied by a slightly delayed appearance of new bands initially located at around 182, 668, 815, and 849 cm^{-1} at 459 °C, the intensity of which increases with temperature. Spectra taken at 716 °C contain additional broad bands at around 351, 598, and 951 cm^{-1} (HT data, Fig. 7a). All newly formed bands survive up to 871 °C except of the bands at 182, 351, and 668 cm^{-1} , which lose their intensity above 768 °C. Chrysotile-like features still observable in situ at 871 °C are the modes at 233.3 cm^{-1} (RT) and 691.3 cm^{-1} (RT), although there are more striking in the subsequently quenched spectrum measured at 47 °C (Fig. 7b).

In situ monitoring of the integral intensity of individual OH

bands would be an elegant technique to obtain structural details of the dehydroxylation process. Unfortunately the resolution both in the HT FTIR and the Raman spectra does not allow proper deconvolution of the individual overlapping OH bands. Therefore, the dehydroxylation progress was monitored by changes in integral intensity/absorbance of the entire OH band region only. The HT FTIR data set shows a sharp decrease in the integral absorbance starting at around 580 °C (Fig. 9a) and going down to less than 10% of the initial value (corresponds approximately to the detection limit for the entire OH bands) at 650 °C. This reduction coincides with the decrease in integral intensity of the Raman OH bands observed in both the HT and quenched spectra (Figs. 9b–9c), although a first decrease in OH band intensity is already visible between 304 and 356 °C. The temperature range in the FTIR data between onset (at around 580 °C) and offset (at around 650 °C) of the dehydroxylation

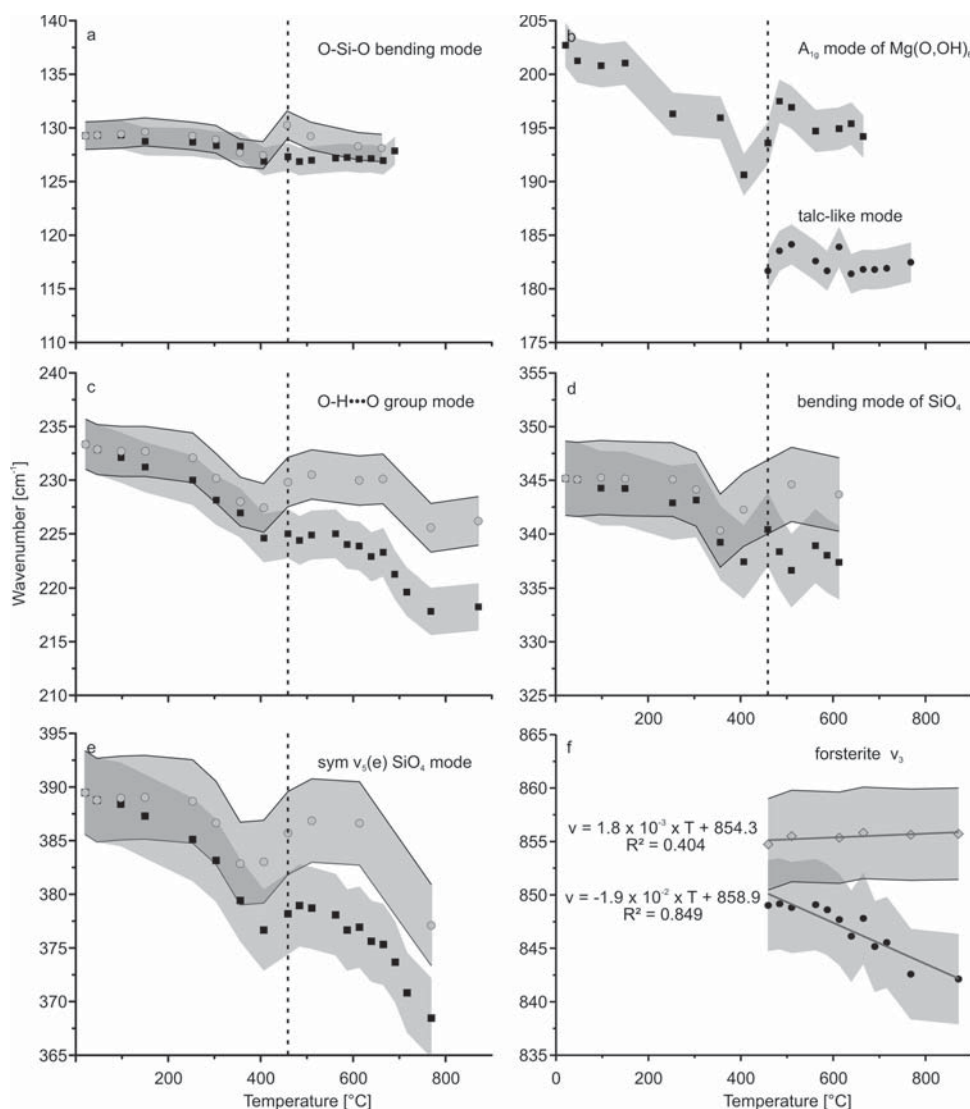


FIGURE 8. Frequency evolution of the major Raman bands during heating; the error envelope is gray shaded. Major error sources are band deconvolution and accuracy of the spectrometer calibration; the vertical dotted line marks the appearance of forsterite bands; reversible shifts as based on quenched data are indicated by the filled circles and their error range (gray shaded area with a black outline).

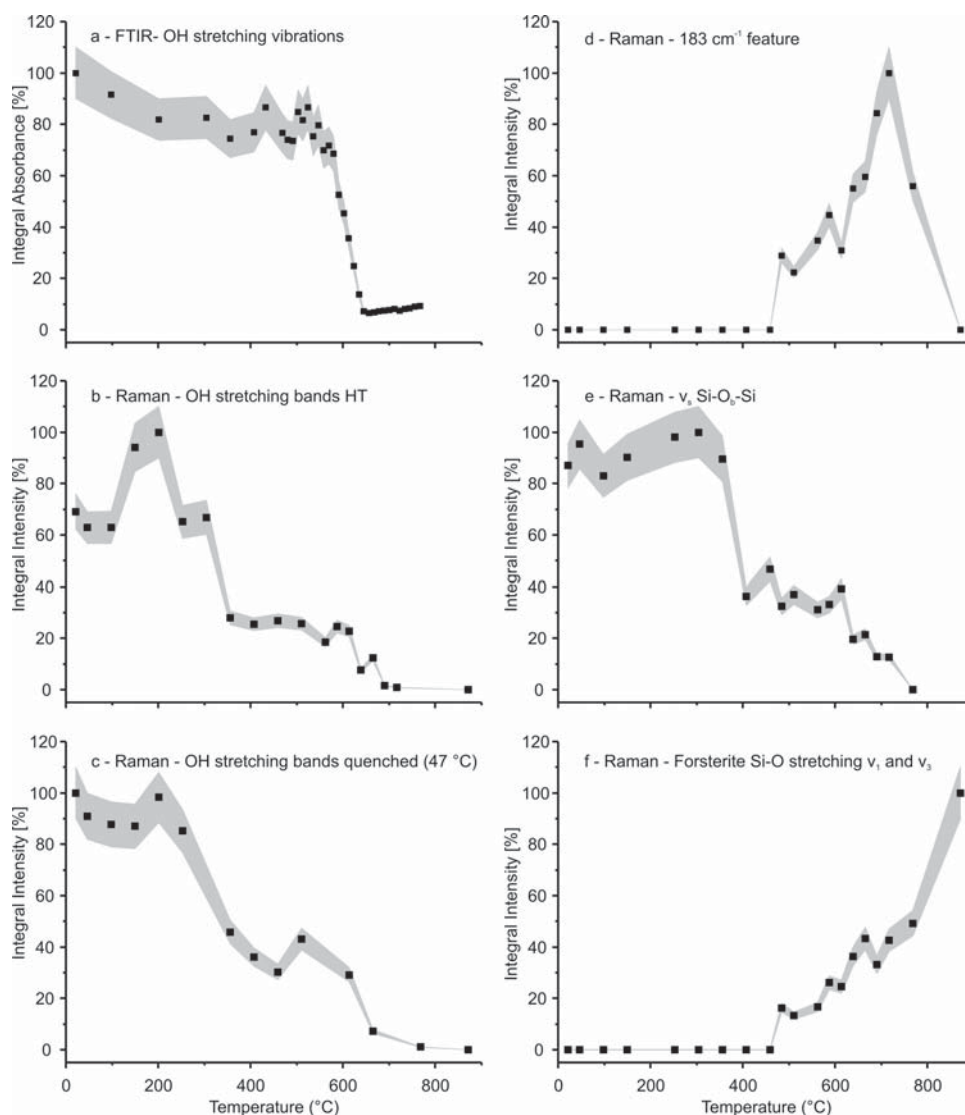


FIGURE 9. Temperature-dependent development of the OH IR band absorbance and integral intensities of some selected Raman bands (gray shading: error envelope).

is much narrower than in DTG data (e.g., Viti 2010), which is typically separated by an interval of more than 200 K independent of the chosen heating rate. The loss of intensity/absorbance is accompanied by a significant non-linear shift toward lower wavenumbers in both FTIR and Raman data. The total shift amounts to about 32 cm^{-1} for the strongest OH Raman band at 3697 cm^{-1} . Compared with the quenched data set, HT data of the OH stretching region contain no clear indication for the appearance of a newly formed OH band.

FTIR and Raman spectroscopy of quenched samples

Spectra were also obtained from samples quenched to $47\text{ }^{\circ}\text{C}$ after reaching the set temperature of the thermal treatment (see methods section) to improve the signal-to-noise ratio and the band resolution. Thus, it was possible to identify weak bands and band splitting much easier than in situ at high temperatures. A

comparison between the HT and quenched data set can be done by using Figures 7a and 7b. Here, weak bands of newly formed phases and remaining bands of a dehydroxylating chrysotile stand out much better (Table 2). Moreover, quenched spectra facilitate band assignments by comparison with Raman database entries (Fig. 10) and help to deconvolute and assign weak bands appearing as shoulders only.

Spectra of quenched samples confirm the appearance of new bands, e.g., at 182 , 669 , and 822 cm^{-1} . In spectra from quenched samples they already appear at lower temperatures than in HT spectra. The splitting of the $\text{Si-O}_6\text{-Si}$ is also better resolved. Inspection of the OH stretching vibrations reveals a band splitting or at least an increase in intensity at the low-frequency shoulder or the major chrysotile OH band. Above $665\text{ }^{\circ}\text{C}$, the low-frequency shoulder turns into a narrow single OH band centered at 3677 cm^{-1} at the expense of primary chrysotile modes (Fig. 11a).

This band is most striking in the quenched spectrum measured at 47 °C after reaching 768 °C, but is already visible at 665 °C.

DISCUSSION

Raman and FTIR spectra at ambient conditions

The number and frequency position of Raman bands in the low-frequency range (Table 1, Fig. 4) agrees well with literature data of chrysotile (e.g., Bard et al. 1997; Klopogge et al. 1999; Rinaudo et al. 2003; Auzende et al. 2004). However, Klopogge et al. (1999) list additional Raman bands at 374, 607, 629, and 709 cm^{-1} originating from band deconvolution in the low-frequency range. Considering the degrees of freedom in choosing the parameters for band deconvolution as shown for chrysotile OH bands by Mizukami et al. (2007) it would also be possible to fit the 389.4 and 623.3 cm^{-1} single bands in our data as potential double bands or even triplets, respectively. The Raman band doublet at 705 and 709 cm^{-1} in the data of Klopogge et al. (1999) might be due to the measurement geometry. The spectra were obtained from crystallographically oriented samples. The chrysotile fibers in the present samples have arbitrary orientation and orientation dependent features were not considered in this study.

The assignments of the chrysotile low-frequency bands (Table 1) were taken from Klopogge et al. (1999) because of almost all recent papers dealing with Raman band assignments of serpentine minerals going back to this article or the paper of Rinaudo et al. (2003). The latter uses the assignments of Klopogge et al. (1999) for other serpentine minerals also. However, band assignments of serpentine minerals are not straightforward and have to be taken with care considering the considerable discrepancies between the assignment schemes presented in previous investigations (Luys et al. 1982; Klopogge et al. 1999; Rinaudo et al. 2003; Hofmeister and Bowey 2006; Šontevska et al. 2007; Prencipe et al. 2009). A good example for such discrepancies are the diagnostic Raman bands between 620 and 635 cm^{-1} observed in experimental spectra of lizardite-1T and chrysotile. These are assigned as antisymmetric OH-Mg-OH translation modes of lizardite and chrysotile by Rinaudo et al. (2003). But, Luys et al. (1982) assigned these bands to in-plane $\text{Mg}(\text{O},\text{OH})_6$ stretching modes originating from curved TO layers. The fact that these bands do not appear in the calculated spectrum of lizardite-1T by Prencipe et al. (2009) is in favor of the latter interpretation. Therefore, the occurrence of 630 and 635 cm^{-1} bands in Raman spectra of lizardite and antigorite presented by Rinaudo et al. (2003), is

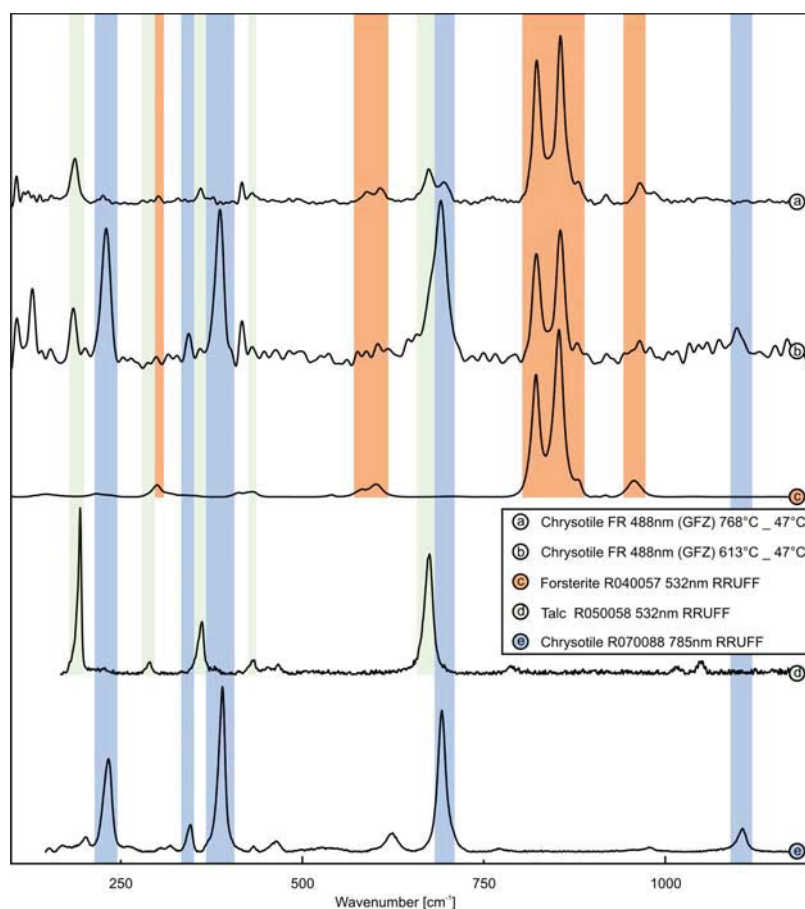


FIGURE 10. Raman spectra of quenched samples after being heated to 613 and 768 °C, respectively, as well as reference spectra of forsterite, talc, and chrysotile from the RRUFF database (Downs 2006).

TABLE 2. Observable Raman modes of chrysotile quenched down to 47 °C after being heated to 613 and 768 °C

Band assignments	613–47 °C (cm ⁻¹)	768–47 °C (cm ⁻¹)	Chrysotile R070088 785 nm** (cm ⁻¹)	Talc R050058 532 nm** (cm ⁻¹)	Forsterite R040057 532 nm** (cm ⁻¹)
O-Si-O bending mode*†‡	128.3		n.p.		
Mg-OH#	184.7	186.7		194.2	
A _{1g} mode of Mg(O,OH) ₆ *†‡	200.5		201.6		
Vibrations of O3-H3...O2*†‡	229.9	225.7	232.9		
Mg ₂ ± y; SiO ₄ ± xy rot. z§		302.1			299.9
Bending of SiO ₄ *†‡	344.2		346.1		
not assigned#	359.2	359.6		362.0	
s ν ₃ (e)SiO ₄ *†‡	387.3		390.2		
n.a.§		588.8			582.1
ν ₄ §		609.6			601.7
Si-O-Si bending#	669.1	673.9		675.3	
ν ₂ Si-O ₂ -Si*†‡	690.9	695.4	692.3		
Mg-OH outer s translation modes*†‡	715.2		708.6		
Si-O stretch ν ₃ §	822.5	823.3			821.9
Si-O stretch, SiO ₄ breathing ν ₃ §	855.4	855.6			853.5
ν ₂ §	878.0	880.6			879.5
ν ₃ §		917.4			917.5
Si-O stretch, SiO ₄ breathing ν ₃ §		967.5			957.3
ν _{as} Si-O _{nb} *†‡	1098.9		1106.4		

Notes: Chrysotile, talc and forsterite modes from database entries are shown for comparison. as = antisymmetric, s = symmetric, b = bridging, nb = non-bridging, n.a. = not assignable when using McKeown et al. (2010), due to different Raman modes in this range, n.p. = not present.

* Rinaudo et al. (2003).

† Farmer (1974).

‡ Klopogge et al. (1999).

§ McKeown et al. (2010).

Fumagalli et al. (2001).

** Downs (2006).

probably related to chrysotile impurities and/or the presence of curled lizardite as observed by Trittschack et al. (2012).

Wavenumber differences between the Raman bands of chrysotile and lizardite-1T are minor, especially when compared with the equivalent differences in the IR spectra of both polymorphs (Yariv and Heller-Kallei 1975), which are more distinct. Differences $\Delta \leq 1$ cm⁻¹ are interpreted as related to measurement errors and/or the band fitting procedure and thus only differences $\Delta \geq 1$ cm⁻¹ are considered. Band displacement resulting from different Raman laser wavelengths as suggested by Šontevska et al. (2007) can be excluded because of the same Raman system used for the previous analysis of lizardite (Trittschack et al. 2012) and the present chrysotile measurements. Difference $\Delta \geq 1$ cm⁻¹ may be caused either by substitution (Farmer 1974; Yariv and Heller-Kallei 1975) or by the structural differences between lizardite and chrysotile. Structural differences are both long-range scale, i.e., flat lizardite vs. curved chrysotile, and short-range scale, i.e., distortion of polyhedra (Blaha and Rosasco 1978). Considering the almost end-member stoichiometry of both the chrysotile used for this investigation and the lizardite-1T studied by Trittschack et al. (2012), we tend to associate the observed differences with the contrasting structures of both phases. It is interesting to note that the largest differences are observed for bands representing tetrahedral units. In this context, the assignment of chrysotile bands at 301.7, 317.5, and 345.2 cm⁻¹ is disputed. Klopogge et al. (1999) attribute these bands to bending modes of SiO₄, whereas Hofmeister and Bowey (2006) assign them to Mg-O stretching modes. Their common negative shift compared to the frequencies observed in lizardite speaks for a common structural origin, i.e., all are either tetrahedral or octahedral modes. The large shift is rather in favor of modes in the tetrahedral sheet.

There are also discrepancies in the number, frequencies, and assignments of OH stretching modes presented in previous FTIR

and Raman investigations of serpentine minerals (Klopogge et al. 1999; Balan et al. 2002; Auzende et al. 2004; Mizukami et al. 2007; Prencipe et al. 2009; Trittschack et al. 2012). In general, older literature document just two IR active bands at 3651 and 3697 cm⁻¹ (Farmer 1974) and two Raman active bands at around 3685 and 3700 cm⁻¹ (Bard et al. 1997), respectively. These findings are mostly caused by the lack of band deconvolution. In recent literature, more bands in chrysotile spectra were reported and assignments were done using the schemes established for lizardite (Balan et al. 2002). Group theory considerations give four Raman active OH stretching vibrations for lizardite-1T (C_{3v} factor group). First-principle calculations of Balan et al. (2002) and Prencipe et al. (2009) result in three IR active OH stretching modes and three Raman active modes plus a contribution of one longitudinal-optical (LO) mode of lizardite-1T, respectively. A higher number of modes than in lizardite are to be expected due to the curved layers and a higher degree of disorder in chrysotile (Devouard and Baronnet 1995; Auzende et al. 2004). The OH stretching band assignments used in this work are in accordance with the scheme proposed for lizardite by Balan et al. (2002). This scheme was already used for high-pressure Raman spectra of chrysotile (Auzende et al. 2004; Mizukami et al. 2007), the ambient spectra of which are comparable to the present ones. Narrow bands in the high frequency side of the Raman OH bands, i.e., at 3681 and 3688 cm⁻¹, are attributed to LO-TO splitting of the in-phase stretching mode of the inner-surface OH groups as proposed by Prencipe et al. (2009). The same splitting was experimentally documented for lizardite-1T by Trittschack et al. (2012). However, as already mentioned, there is a high degree of freedom when applying band deconvolution techniques [see Mizukami et al. (2007)]. Thus, only state-of-the-art ab initio techniques are suited to unravel the exact number of vibrational bands considering the influence of substitution, crystal defects or

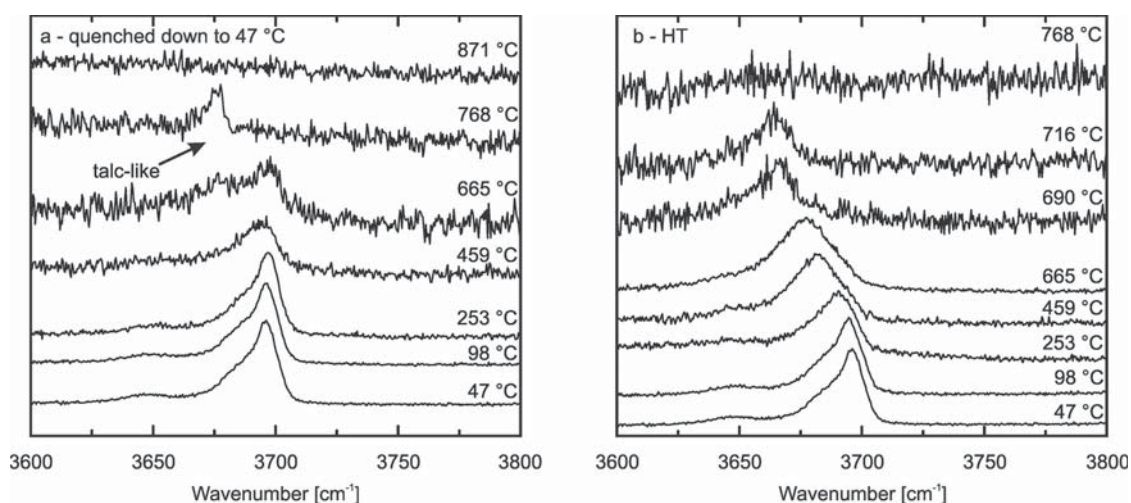


FIGURE 11. Temperature-dependent changes in the Raman OH stretching band region. (a) Measured on samples quenched from the indicated temperature and (b) HT spectra measured at the indicated temperatures.

such physical influences like LO-TO splitting. The two adjacent IR bands at 3695 and 3702 cm^{-1} are probably caused by a minor substitutional exchange of Mg by Fe (Yariv and Heller-Kallei 1975) or a distortion of the SiO_4 tetrahedra (Blaha and Rosasco 1978). LO-TO splitting as cause for an OH band multiplication in FTIR data can be excluded due to the size of individual chrysotile fibers with respect to the IR wavelength range. A band occurring between the out-of-phase stretching and the in-phase stretching mode of the inner-surface OH, which is not present in the Balan et al. (2002) scheme, was already observed in spectra of lizardite-1T (Trittschack et al. 2012). This band has been attributed to non-structural OH in the case of lizardite, although a deconvolution artifact cannot be excluded (Trittschack et al. 2012).

The chrysotile phase transformation as seen in the OH stretching band range

The dehydroxylation of chrysotile as deduced from the decrease in integral absorbance/intensity of OH stretching modes (Figs. 9a–9c) starts approximately at the same temperature as the onset of the weight loss in published differential thermogravimetric (DTG) data of chrysotile (Viti 2010). However, the total dehydroxylation interval in spectroscopic data is much narrower than that recorded by DTG, a fact already observed in the dehydroxylation of lizardite (Trittschack et al. 2012). This difference is related to the nature of the measured signals, i.e., debonding of hydroxyl groups lead to the signal decrease in FTIR/Raman data, whereas the diffusion of reaction products out of the sample is responsible for the weight loss in the solid sample, which is monitored by DTG. The latter is delayed relative to the hydroxyl debonding reactions. The stepwise decrease in Raman intensity as recognizable from the OH Raman bands (Figs. 9b and 9c) demonstrates a more complex reaction path than observable by FTIR alone. Thus, we suggest two interpretation models for the herein documented Raman band changes that are linked to each other: (1) A decrease in the integral OH Raman intensity at temperatures lower than 400 °C could be caused by temperature-induced reorientation of single chrysotile fibers within the fiber bundle as the intensity of OH Raman bands is

also a function of the fiber orientation (Klopprogge et al. 1999). (2) An early order/disorder phase transition in the outer, less temperature resistant chrysotile layers is also possible. Such an interpretation would partly support the interpretation of Candela et al. (2007) who suggest an increase in the degree of order at temperatures between 400 and 450 °C. Interestingly, Cattaneo et al. (2003) also document a slight increase in their summed integrated XRD peak intensity between 400 and 500 °C, which can also be interpreted as an indication for increased order. However, in any case such a transition would also cause reorientation of OH and therefore a change in the Raman intensity. Moreover, Malkov et al. (2009) document an early release of OH in the temperature range of 20 to 400 °C. Their calculations yield a loss in OH of almost 2 mmol/g, which is equal to around 12.7% of the initial amount of OH.

Generally, the chrysotile structure and in particular the average curvature changes during dehydroxylation. The dehydroxylation temperature of the individual chrysotile layers is radius-dependent, i.e., the outer, less curved layers, dehydroxylate at lower temperatures than the inner ones (Evans 2004). As long as the maximum experimental temperature is lower than the onset of the dehydroxylation in the outermost layer, the average curvature in the quenched samples is equal to the value in the starting sample. This assumption is fulfilled as shown in Figure 11. Accordingly, a broadening of the OH stretching region in HT and quenched data are expected after the onset of the dehydroxylation resulting from progressive disorder moving inward. Then, the resulting OH mode pattern would consist of OH modes coming from the primary chrysotile and a disordered one. This assumption can also be verified by the presented OH band development in Figure 11 showing a comparable OH band pattern up to 253 °C with respect to the initial sample. Although diminishing in intensity, the position of the main OH band at 3697 cm^{-1} keeps fixed (in quenched data) as long as the inner chrysotile layers are not affected by dehydroxylation. Afterward a significant broadening can be detected in both HT and quenched data (Fig. 11), respectively.

A rather simple model of chrysotile as shown by D'Arco et

al. (2009) enables us to use a compatible dehydroxylation model as for lizardite-1T (Trittschack and Grob ty 2012). There, the distance between adjacent OH groups in lizardite-1T counts as a trigger for a preferential loss of protons and finally causing disorder and creating a host for a potential intermediate phase. The appearance of a new OH band at 3677 cm^{-1} (quenched sample), which is the only visible OH stretching band after heating the sample to $768\text{ }^\circ\text{C}$, is an indication for the formation of an intermediate phase other than the ill-crystallized primary product and forsterite. This single OH band is compatible with the OH band position of talc at RT (Fumagalli et al. 2001), an interpretation strongly supported by newly formed bands in the low-frequency range and discussed in detail in the following section. The lack of this OH band at $871\text{ }^\circ\text{C}$ and in the spectrum of the subsequently quenched sample indicates that this intermediate breaks down between 768 and $871\text{ }^\circ\text{C}$.

The chrysotile phase transformation as seen in the low-frequency range ($100\text{--}1200\text{ cm}^{-1}$)

Frequency shifts, intensity loss and appearance of new bands also characterize the low-frequency range of both quenched samples and HT spectra independent of the temperature of the heat treatment (Figs. 6–9). Considering the small difference between the frequencies observed in chrysotile compared to lizardite (Fig. 4, Table 1), the influence of the curvature on the frequency of individual bands seems to be small. The measurement errors related to sample refocusing due to the thermal expansion of the sample holder and the chrysotile itself are not helping in determining small permanent frequency shifts. The layer volume corresponding to a certain curvature decreases with increasing curvature, e.g., the overall impact on the spectra of the outer, less curved layers is larger than that of the inner layers.

The local frequency minima at 356 and $407\text{ }^\circ\text{C}$ and the following plateau are interpreted as a first step in the phase transformation that takes place in the outer, less curved layers. This is again in favor with the findings of Candela et al. (2007). But, comparable experiments by Gualtieri et al. (2012) have not confirmed such a behavior. Nevertheless, the local minima observable in the low-frequency Raman bands are supported by the first significant decrease in the integral intensities of OH Raman bands between 304 and $356\text{ }^\circ\text{C}$ (Figs. 6, 7, and 9). The apparent loss of OH and the significant step to lower wavenumbers might be interpretable as a loss of primary chrysotile features. But, a recrystallization to a chrysotile with different radii at higher temperatures as proposed by Candela et al. (2007) seems to be problematic due to the loss of primary OH. Unfortunately, there is no further literature on the phase transformation and dehydroxylation behavior of chrysotile supporting such low-temperature ($T < \sim 450\text{ }^\circ\text{C}$) recrystallization effects, which could also support a better understanding of our own data.

The overall phase change is not restricted to a narrow temperature interval like in lizardite, but a broad temperature range with a “transition” zone between 407 and $768\text{ }^\circ\text{C}$ (Figs. 6 and 7a–7b). The maximum stability temperature of chrysotile is in accordance with recently published data (Gualtieri et al. 2012). This transition zone is characterized by the coexistence of chrysotile, a “disordered chrysotile” plus a quenchable talc-like phase and forsterite as interpreted from the wavenumber positions of quenched

samples at $47\text{ }^\circ\text{C}$ (Table 2, Fig. 10). The “disordered chrysotile” is an almost OH free phase containing remnants of the primary structure as interpreted from missing hydroxyl bands, but still appearing chrysotile-compatible bands in the low-frequency range (Figs. 6, 7b, 8c, and 10). Such an OH-poor, amorphous phase occurred also during the dehydroxylation of lizardite (McKelvy et al. 2006, Trittschack et al. 2012). The most striking band of the talc-like intermediate lies at 184.7 cm^{-1} followed by less intense bands at 359.2 and 669.1 cm^{-1} (Figs. 7a–7b and 10). It is labeled as “talc-like” due to the deviations of measured Raman modes when comparing them with those reported for talc in literature (Table 2, Downs 2006). Moreover, there are no clear evidences in previous XRD based literature for the presence of talc, but the appearance of a talc-like and rapidly changing $10\text{+ } \text{Å}$ peak. Forsterite can easily be identified by the remarkable doublet at 823 and 856 cm^{-1} and a smaller doublet at 589 and 607 cm^{-1} (Figs. 7a–7b and 10). The appearance of an intermediate phase during the “dry” dehydroxylation of chrysotile is compatible with existing reaction schemes (Ball and Taylor 1963; Brindley and Hayami 1965; Martin 1977; Datta 1991). The talc-like character was first proposed by MacKenzie and Meinhold (1994) based on NMR analysis. Gualtieri et al. (2012) and Trittschack et al. (2012) have also found evidence of a talc-like phase in in situ HT X-ray powder diffraction and Raman spectra of partially dehydroxylated lizardite. The presence of a talc-like intermediate is not surprising as talc is a stable product during the breakdown of chrysotile and lizardite under hydrothermal conditions (Ball and Taylor 1963; O’Hanley et al. 1989). MacKenzie and Meinhold (1994) explained the appearance of a talc-like intermediate with the possibility of quasi-hydrothermal conditions in the innermost layers of chrysotile. Such conditions might not be limited to the innermost layers as demonstrated by the first appearance of talc-like features at $459\text{ }^\circ\text{C}$ (Figs. 7a–7b and 9d), i.e., early after the Raman/FTIR detectable onset of dehydroxylation (Figs. 9a–9c) and the DTG detectable onset of dehydration (Viti 2010). What can be stated at this point is that hydrothermal conditions have to be achieved in certain parts of the changing host-structure during the dehydroxylation of chrysotile and lizardite. The formation of a disordered, OH-free chrysotile intermediate inhibiting the diffusion of H_2O or OH might be the reason for a locally enrichment of volatile dehydroxylation products.

The accelerated growth of the talc-like intermediate at temperatures $\geq 613\text{ }^\circ\text{C}$ is mirrored by a strong decrease in the intensity of chrysotile bands (Figs. 9d and 9e). This behavior implies an immediate nucleation and growth of the talc-like phase during the dehydroxylation. Owing to the contemporaneous appearance of the talc-like phase and forsterite at $459\text{ }^\circ\text{C}$ it is not possible to state whether the intermediate is necessary or not to form forsterite. However, the accelerated increase in intensity of the Si-O stretching mode doublet of forsterite after the maximum intensity of the talc-like phase at $716\text{ }^\circ\text{C}$ suggest a strong interrelation. The fact that forsterite shows the largest integral intensity at $871\text{ }^\circ\text{C}$ point to an unfinished growth. The breakdown of the talc-like intermediate is not accompanied by the formation of enstatite as proposed for antigorite by Gualtieri et al. (2012). The absence of enstatite is either related to an unfinished breakdown of the chrysotile structure preventing a formation of the inosilicate or kinetic effects in general. However, both pos-

sibilities are linked to each other as the chrysotile breakdown itself is a time-dependent, i.e., kinetic-controlled, reaction (Candela et al. 2007). The exposure time at $T \geq 800$ °C is less than 10 min, which is also not favorable for a formation of enstatite. The formation of a Si-rich amorphous phase as dehydroxylation product as inferred from in situ X-ray diffraction (Ball and Taylor 1963; Martin 1977; MacKenzie and Meinhold 1994; Gualtieri et al. 2012) is difficult to prove by the present spectroscopic data, as all Raman bands in the HT and quenched spectra can be assigned to known crystalline phases, i.e., talc-, chrysotile-, and forsterite-related modes. The broadened chrysotile bands point to a decrease in crystallinity and what was called amorphous phase by previous authors is rather a heavily disordered phase still resembling chrysotile. Such a disordered chrysotile phase might be similar to the dehydroxylate II using the nomenclature of MacKenzie and Meinhold (1994). The latter argue that the NMR shift of this dehydroxylated II is compatible with a 1:1 layer structure of chrysotile in general, i.e., dehydroxylated II is still containing elements of the primary chrysotile structure, although disordered. They also demonstrate its presence above 800 °C, which is compatible with the herein documented data. However, MacKenzie and Meinhold (1994) suggest either a phase similar to talc or a phase still containing structural elements of chrysotile for their dehydroxylated II. Their phrases exclude therefore an unambiguous assignment.

The frequency change of the O-Si-O bending mode (~ 129 cm^{-1} at RT), which is a measure of the change in ditrigonal distortion α (Mookherjee and Redfern 2002), is nearly one order of magnitude smaller than the rest of the chrysotile bands. Weak dependency of α on temperature was already observed for lizardite-1T upon heating as shown by HT Raman (Trittschack et al. 2012) and XRD studies (Guggenheim and Zhan 1998). The possibility to fit the O-Si-O bending mode with just one band with nearly constant FWHM upon the entire temperature range suggests no or minor influence of the layer curvature on α .

Chrysotile fibers are characterized by an inward migrating dehydroxylation surface according to the proposed chrysotile structures of Yada (1971) and thermodynamic considerations given by Evans (2004). This surface would generate a “chrysotile” fiber consisting of three or four different phases, respectively (Fig. 12). However, the variability in the fiber diameter of the studied chrysotile causes a more complex situation. Nevertheless, the principle scheme maintains.

It is necessary to underline that the talc-like intermediate is quenchable during the breakdown of chrysotile. Thus, the intermediate is an important carrier of H_2O and OH, respectively. This has to be considered when interpreting the kinetics of the chrysotile dehydroxylation by DTG, a statement also valid for all other phyllosilicates creating an H_2O /OH containing intermediate phase during dehydroxylation. In any case, the chrysotile dehydroxylation is not that linear as assumed in the past, which has already demonstrated by experiments of Viti (2010) indicating a multistage dehydration process. The FTIR and Raman data of this article clearly show a multistage dehydroxylation and phase transformation scenario with an early onset of a possible order/disorder phase transition at temperatures between around 350 and 450 °C, followed by the main dehydroxylation reaction and phase change later on. However, the low temperature of the

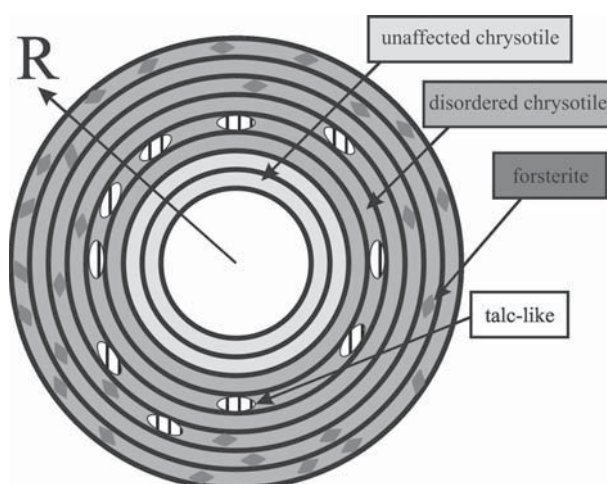


FIGURE 12. Schematic representation of a dehydroxylating chrysotile fiber (concentric type) with a multiphase assemblage of unaffected chrysotile, disordered chrysotile, the talc-like phase and forsterite; the talc-like phase is shown as formed on certain areas of the disordered chrysotile only, R = fiber radius.

first appearance of the talc-like phase and forsterite compared to the temperatures of the first release of water in data of Viti (2010) demonstrate that one has to be careful with a direct comparison of both data sets. It has to be emphasized that a multistage dehydration is not inevitably caused by a multistage dehydroxylation reaction.

The occurrence of a talc-like intermediate stable under ambient pressure conditions and the presence of a disordered chrysotile also have an impact on the understanding of subduction zone dehydration processes and the storage of CO_2 in serpentine bearing rocks. The presence of a talc-like phase rather than talc offers the possibility for a transport, storage, and release of H_2O at low-pressure conditions, but after the onset of the temperature-dependent dehydroxylation reaction of chrysotile and lizardite. Much work has been devoted to high-pressure experiments studying the breakdown reaction of antigorite (e.g., Perrillat et al. 2005; Chollet et al. 2009). But, less is documented about the relation of the lizardite and chrysotile breakdown including the formation of a talc-like intermediate. Additional studies are important to unravel the complex association between primary serpentine minerals, the talc-like phase, talc, and the 10 Å phase (Fumagalli et al. 2001; Chollet et al. 2009) in the MSH system. Moreover, a talc-like phase offers potential nucleation sites of carbonate bearing phases in carbon capture and sequestration experiments. Some of our work in progress indicates a delayed decomposition and a shift of the chrysotile breakdown toward higher temperature when not using a purging gas. Thus, the activity/ $p_{\text{H}_2\text{O}}$ has a major impact on the breakdown and formation conditions of all occurring phases, a fact already demonstrated for high-pressure decomposition reactions of antigorite (Perrillat et al. 2005).

ACKNOWLEDGMENTS

The authors thank two anonymous reviewers for their helpful and constructive comments that improved the quality of the manuscript. Furthermore, we thank the associate editor Roland Stalder. Special thanks goes to Monika Koch-Müller (GFZ Potsdam) and Sergio Speziale (GFZ Potsdam) for the supply of the spectroscopic

facilities and the on-site support as well as Marcello Mellini for providing the Monte Fico sample. This study was funded by the Swiss National Science Foundation (grant 200021-121964 and -140497).

REFERENCES CITED

- Anbalagan, G., Sivakumar, G., Prabakaran, A.R., and Gunasekaran, S. (2010) Spectroscopy characterization of natural chrysotile. *Vibrational Spectroscopy*, 52, 122–127.
- Aruja, E. (1943) An X-ray study of silicates, chrysotile, antigorite, gumbelite. Ph.D. thesis, University of Cambridge, U.K.
- Auzende, A.-L., Daniel, I., Reynard, B., Lemaire, C., and Guyot, F. (2004) High-pressure behaviour of serpentine minerals: a Raman spectroscopic study. *Physics and Chemistry of Minerals*, 31, 269–277.
- Balan, E., Saitta, A.M., Mauri, F., Lemaire, C., and Guyot, F. (2002) First-principles calculation of the infrared spectrum of lizardite. *American Mineralogist*, 87, 1286–1290.
- Ball, M.C. and Taylor, H.F.W. (1963) The dehydration of chrysotile in air and under hydrothermal conditions. *Mineralogical Magazine*, 33, 467–482.
- Bard, D., Yarwood, J., and Tylee, B. (1997) Asbestos fibre identification by Raman microspectroscopy. *Journal of Raman spectroscopy*, 28, 803–809.
- Blaha, J.J. and Rosasco, G.J. (1978) Raman microprobe spectra of individual microcrystals and fibers of talc, tremolite, and related silicates minerals. *Analytical Chemistry*, 50, 892–896.
- Brindley, G.W. and Hayami, R. (1963a) Kinetics and mechanisms of dehydration and recrystallization of serpentine-I. *Clays and Clay Minerals*, 12, 35–47.
- (1963b) Kinetics and mechanisms of dehydration and recrystallization of serpentine-II, spectrum of activation energies for recrystallization. *Clays and Clay Minerals*, 12, 49–54.
- (1965) Mechanism of formation of forsterite and enstatite from serpentine. *Mineralogical Magazine*, 35, 189–195.
- Brindley, G.W. and Zussman, J. (1957) A structural study of the thermal transformation of serpentine minerals to forsterite. *American Mineralogist*, 42, 461–474.
- Candela, P.A., Crummett, C.D., Earnest, D.J., Frank, M.R., and Wylie, A.G. (2007) Low-pressure decomposition of chrysotile as a function of time and temperature. *American Mineralogist*, 92, 1704–1713.
- Cattaneo, A., Gualtieri, A.F., and Artoli, G. (2003) Kinetic study of the dehydroxylation of chrysotile asbestos with temperature by in situ XRPD. *Physics and Chemistry of Minerals*, 30, 177–183.
- Chollet, M., Daniel, I., Koga, K.T., Petigirard, S., and Morard, G. (2009) Dehydration kinetics of talc and 10 Å phase: consequences for subduction zone seismicity. *Earth and Planetary Science Letters*, 284, 57–64.
- Cressey, G., Cressey, B.A., and Wicks, F.J. (2008) Polyhedral serpentine: a spherical analogue of polygonal serpentine?. *Mineralogical Magazine*, 72, 1229–1242.
- D'Arco, P., Noel, Y., Demichelis, R., and Dovesi, R. (2009) Single-layered chrysotile nanotubes: A quantum mechanical ab initio simulation. *Journal of Chemical Physics*, 131, 204701.
- Datta, A.K. (1991) Dehydration of chrysotile asbestos—an infrared-absorption study. *Journal of Materials Science Letters*, 10, 870–871.
- Datta, A.K., Mathur, B.K., Samantaray, B.K., and Bhattacharjee, S. (1987) Dehydration and phase transformation on chrysotile asbestos—a radial distribution analysis study. *Bulletin of Material Science*, 9, 103–110.
- Devouard, B. and Baronnat, A. (1995) Axial diffraction of curved lattices: geometrical and numerical modeling. Application to chrysotile. *European Journal of Mineralogy*, 7, 835–846.
- Dódony, I. and Buseck, P.R. (2004) Serpentine close-up and intimate: an HRTEM view. *International Geology Review*, 46, 507–527.
- Downs, R.T. (2006) The RRUFF Project: an integrated study of the chemistry, crystallography, Raman and infrared spectroscopy of minerals. Program and Abstracts of the 19th General Meeting of the International Mineralogical Association in Kobe, Japan, O03-13.
- Evans, B.W. (2004) The serpentinite multisystem revisited: chrysotile is metastable. *International Geology Review*, 46, 479–506.
- Farmer, V.C., Ed. (1974) *The Infrared Spectra of Minerals*. Mineralogical Society, London.
- Fuchs, Y., Linares, J., and Mellini, M. (1998) Mössbauer and infrared spectrometry of lizardite-1T from Monte Fico, Elba. *Physics and Chemistry of Minerals*, 26, 111–115.
- Fumagalli, P., Stixrude, L., Poli, S., and Snyder, D. (2001) The 10 Å phase: a high-pressure expandable sheet silicate stable during subduction of hydrated lithosphere. *Earth and Planetary Science Letters*, 186, 125–141.
- Grobóty, B. (2003) Polytypes and higher-order structures of antigorite: a TEM study. *American Mineralogist*, 88, 27–36.
- Gualtieri, A.F., Giacobbe, C., and Viti, C. (2012) The dehydroxylation of serpentine group minerals. *American Mineralogist*, 97, 666–680.
- Guggenheim, S. and Zhan, W. (1998) Effect of temperature on the structures of lizardite-1T and lizardite-2H. *Canadian Mineralogist*, 36, 1587–1594.
- Hey, M.H. and Bannister, F.A. (1948) A note on the thermal decomposition of chrysotile. *Mineralogical Magazine*, 28, 333–337.
- Hofmeister, A.M. and Bowey, J.E. (2006) Quantitative infrared spectra of hydrosilicates and related minerals. *Monthly Notices of the Royal Astronomical Society*, 367, 577–591.
- Jolicoeur, C. and Duchesne, D. (1981) Infrared and thermogravimetric studies of the thermal-degradation of chrysotile asbestos fibers: evidence for matrix effects. *Canadian Journal of Chemistry*, 59, 1521–1526.
- Klopprogge, J.T., Frost, R.L., and Rintoul, L. (1999) Single crystal Raman microscopic study of the asbestos mineral chrysotile. *Physical Chemistry Chemical Physics*, 1, 2559–2564.
- Long, D.A. (1977) *Raman Spectroscopy*. McGraw-Hill, New York.
- Luys, M.-J., De Roy, G., Vansant, E.F., and Adams, F. (1982) Characteristics of asbestos minerals. *Journal of the Chemical Society, Faraday Transactions I*, 78, 3561–3571.
- MacKenzie, K.J.D. and Meinhold, R.H. (1994) Thermal reactions of chrysotile revisited: A ²⁹Si and ²⁵Mg MAS NMR study. *American Mineralogist*, 79, 43–50.
- Malkov, A.A., Korytkova, E.N., Maslennikova, T.P., Shtykhova, A.M., and Gusarov, V.V. (2009) Effect of heat treatment on structural-chemical transformations in magnesium hydrosilicate [Mg₃Si₂O₅(OH)₂] nanotubes. *Russian Journal of Applied Chemistry*, 82, 2079–2086.
- Martin, C.J. (1977) The thermal decomposition of chrysotile. *Mineralogical Magazine*, 41, 453–459.
- McKelvy, M.J., Chizmeshya, A.V.G., Diefenbacher, J., Béarat, H., and Wolf, G. (2004) Exploration of the role of heat activation in enhancing serpentine carbon sequestration reactions. *Environmental Science and Technology*, 38, 6897–6903.
- McKelvy, M.J., Sharma, R., and Chizmeshya, A.V.G. (2006) Lamellar reaction phenomena: from intercalation to nanomaterials formation. *Journal of Physics and Chemistry of Solids*, 67, 888–895.
- McKeown, D.A., Bell, M.I., and Caracas, R. (2010) Theoretical determination of the Raman spectra of single-crystal forsterite (Mg₂SiO₄). *American Mineralogist*, 95, 980–986.
- Mellini, M. and Viti, C. (1994) Crystal-structure of lizardite-1T from Elba, Italy. *American Mineralogist*, 79, 1194–1198.
- Mizukami, T., Kagi, T., Wallis, S.R., and Fukura, S. (2007) Pressure-induced change in the compressional behavior of the O-H bond in chrysotile: A Raman high-pressure study up to 4.5 GPa. *American Mineralogist*, 92, 1456–1463.
- Mookherjee, M. and Redfern, S.A.T. (2002) A high-temperature Fourier transform infrared study of the interlayer and Si-O-stretching region in phengite-2M₁. *Clay Minerals*, 37, 323–336.
- O'Hanley, D.S., Chernosky, J.V., and Wicks, F.J. (1989) The stability of lizardite and chrysotile. *Canadian Mineralogist*, 27, 483–493.
- Perrillat, J.-P., Daniel, I., Koga, K.T., Reynard, B., Cardon, H., and Crichton, W.A. (2005) Kinetics of antigorite dehydration: a real-time X-ray diffraction. *Earth and Planetary Science Letters*, 236, 899–913.
- Post, J.L. and Borer, L. (2000) High-resolution infrared spectra, physical properties, and micromorphology of serpentines. *Applied Clay Sciences*, 16, 73–85.
- Prencipe, M., Noel, Y., Bruno, M., and Dovesi, R. (2009) The vibrational spectrum of lizardite-1T [Mg₃Si₂O₅(OH)₂] at the Γ point: a contribution from an ab initio periodic B3LYP calculation. *American Mineralogist*, 94, 986–994.
- Rinaudo, C., Gastaldi, D., and Belluso, E. (2003) Characterization of chrysotile, antigorite and lizardite by FT-Raman spectroscopy. *Canadian Mineralogist*, 41, 883–890.
- Šontevska, V., Jovanovski, G., and Makreski, P. (2007) Minerals from Macedonia. Part XIX. Vibrational spectroscopy as identification tool for some sheer silicate minerals. *Journal of Molecular Structure*, 834–836, 318–327.
- Trittschack, R. and Grobóty, B. (2012) Dehydroxylation kinetics of lizardite. *European Journal of Mineralogy*, 24, 47–57.
- Trittschack, R., Grobóty, B., and Koch-Müller, M. (2012) In situ high-temperature Raman and FTIR spectroscopy of the phase transformation of lizardite. *American Mineralogist*, 97, 1965–1976.
- Viti, C. (2010) Serpentine minerals discrimination by thermal analysis. *American Mineralogist*, 95, 631–638.
- Wicks, F.J. and O'Hanley, D.S. (1988) Serpentine minerals: structures and petrology. In S.W. Bailey, Ed., *Hydrous Phyllosilicates (Exclusive of Micas)*, 19, p. 91–167. Reviews in Mineralogy, Mineralogical Society of America, Chantilly, Virginia.
- Wicks, F.J. and Whittaker, E.J.W. (1975) A reappraisal of the structures of the serpentine minerals. *Canadian Mineralogist*, 13, 227–243.
- Yada, K. (1971) Study of microstructure of chrysotile asbestos by high resolution electron microscopy. *Acta Crystallographica*, A27, 659–664.
- Yariv, S. and Heller-Kallei, L. (1975) The relationship between the I.R. spectra of serpentines and their structures. *Clays and Clay Minerals*, 23, 142–152.